

Numerical simulations of a cylinder wake under a strong axial magnetic field

Vincent Dousset^{a)} and Alban Pothérat^{b)}

Applied Mathematics Research Centre, Faculty of Engineering and Computing, Coventry University, Priory Street, Coventry CV1 5FB, United Kingdom

(Received 15 May 2007; accepted 15 November 2007; published online 23 January 2008)

We study the flow of a liquid metal in a square duct past a circular cylinder in a strong externally imposed magnetic field. In these conditions, the flow is quasi-two-dimensional, which allows us to model it using a two-dimensional (2D) model. We perform a parametric study by varying the two control parameters Re and Ha (Ha^2 is the ratio of Lorentz to viscous forces) in the ranges $[0 \dots 6000]$ and $[0 \dots 2160]$, respectively. The flow is found to exhibit a sequence of four regimes. The first three regimes are similar to those of the non-magnetohydrodynamic (non-MHD) 2D circular wake, with transitions controlled by the friction parameter Re/Ha . The fourth one is characterized by vortices raising from boundary layer separations at the duct side walls, which strongly disturbs the Kármán vortex street. This provides the first explanation for the breakup of the 2D Kármán vortex street first observed experimentally by Frank, Barleon, and Müller [Phys. Fluids **13**, 2287 (2001)]. We also show that, for high values of Ha ($Ha \geq 1120$), the transition to the fourth regime occurs for $Re \propto 0.56Ha$, and that it is accompanied by a sudden drop in the Strouhal number. In the first three regimes, we show that the drag coefficient and the length of the steady recirculation regions located behind the cylinder are controlled by the parameter $Re/Ha^{4/5}$. Also, the free shear layer that separates the recirculation region from the free stream is similar to a free MHD parallel layer, with a thickness of the order of $Ha^{-1/2}$ that is quite different to that of the non-MHD case, and therefore strongly influences the dynamics of this region. We also present one case at $Re = 3 \times 10^4$ and $Ha = 1120$, where this layer undergoes an instability of the Kelvin–Helmholtz-type. © 2008 American Institute of Physics. [DOI: 10.1063/1.2831153]

I. INTRODUCTION

In nuclear fusion reactors, extremely hot plasma volumes are kept away from the walls of the reactor by an intense magnetic field of the order of 10 Tesla generated by a set of superconducting magnet coils. Liquid metal blankets placed between the reactor and the coils are then designed, among other goals, to evacuate heat away from the reactor so as to control its temperature. Yet, the imposed magnetic field is so intense that it modifies turbulence in the flow, which causes a dramatic reduction in the heat transfer rate. In order to promote turbulence, obstacles can be placed inside the blanket. This technological issue is the one of the main motivations for studying the magnetohydrodynamic (MHD) flow past an obstacle in a strong external magnetic field.

A large amount of work in the literature has been devoted to the study of the non-MHD flow (with no magnetic field) past a circular cylinder whose axis is perpendicular to the streamwise direction. An extensive review is available in Refs. 2 and 3. In an unbounded fluid domain, the flow is governed by only one parameter, the Reynolds number Re which is the ratio of inertial to viscous forces. By increasing Re from 0, one can identify three successive two-dimensional (2D) regimes until the flow becomes three-dimensional (3D) for Re about 190. The first flow regime,

denoted thereafter as **I**, is the creeping flow regime where the main stream remains attached to the cylinder circumference. In the second one (**II**), two steady recirculation regions symmetrically placed on each side of the wake and attached to the rear of the cylinder appear and lengthen as Re is increased. In the last 2D flow regime (**III**), the flow becomes unsteady as an alternate procession of counter-rotating vortices, known as *Kármán vortex street*, develops in the wake.

Compared to this ideal case, the configuration of interest for liquid metal blankets involves two important additional features responsible for extra physical effects. First, the flow is bounded by four impermeable walls, two parallel and two orthogonal to the cylinder axis and second, a strong homogeneous externally applied magnetic field is imposed in the direction of the cylinder axis. The effect of confinement between plates parallel to the cylinder axis has been investigated in Refs. 4–11 for moderate Re values ($Re < 10^3$) without magnetic field. In this configuration, the ratio β , called *blockage ratio*, of the cylinder diameter to the distance between the parallel plates is an additional flow parameter which shifts the transitions between flow regimes to higher Re for $\beta > 0.2$ and causes the appearance of specific flow patterns for $\beta > 0.6$.¹⁰ The presence of an external magnetic field **B** in an electrically conducting flow gives birth to an induced magnetic field and induced electrical currents. When the magnetic Reynolds number R_m is much smaller than 1, as in small liquid metal experiments, the induced magnetic field is negligible, but not the induced currents, and the total mag-

^{a)}Electronic mail: aa4112@coventry.ac.uk.

^{b)}Electronic mail: alban.potherat@coventry.ac.uk.

netic field is the imposed one.¹² The interaction between the induced currents and the magnetic field generates Lorentz forces that tend to damp velocity variations along the streamlines.¹³ If the interaction parameter N and the Hartmann number Ha , which are, respectively, the ratio of Lorentz to inertia forces and the square of that of Lorentz to viscous forces, are large, the flow is invariant along the magnetic field lines, except in the vicinity of the walls that intersect them. In this region, viscous forces maintain strong velocity gradients and the so-called *Hartmann layer* develops. The resulting flow, made of such Hartmann layers and a core flow where the velocity is constant along the magnetic field lines, is called *quasi-two-dimensional* (quasi-2D). The orientation of the magnetic field with respect to the axis of the cylinder is therefore of crucial importance. While the case where \mathbf{B} is oriented along the streamwise direction has received significant attention (experiments in Refs. 14–17 and numerical computations in Refs. 18–20), the literature on flows where \mathbf{B} is aligned with the cylinder axis is scarcer. It has been investigated in experiments from Refs. 1, 14, and 21–24 while, to our knowledge, only Ref. 25 has performed numerical simulations on this configuration but with a square-based cylinder. Reference 1 has experimentally identified four flow regimes: the first three correspond to the 2D ones of the non-MHD flow, while the fourth one is characterized by an irregular Kármán vortex street. The magnetic field shifts the onset of the unsteady flow regime to higher Re ,^{1,21} and the related critical Re increases linearly with Ha .¹ The numerical simulations from Ref. 25 have shown that for moderate interaction parameters ($N < 12$), the vortices parallel to \mathbf{B} are not perfectly 2D in the internal region of the flow, but have a cigar-like shape.

The treatment of the Hartmann layers, that develop along the plates normal to \mathbf{B} , i.e., at the top and bottom of our cylinder, remains the limiting issue for fully 3D numerical investigations and explains their scarcity in the literature. In an intense magnetic field, the Hartmann layers are so thin that the required mesh within these layers involves prohibitive storage and CPU performances. Reference 25 has used an analytical wall function to compute the solution in the Hartmann layers from the results of the computations in the core flow. In spite of this, high Re flows still remain out of reach of such 3D computations.

We propose to tackle this problem for $N \gg 1$ and $Ha \gg 1$ by taking advantage of the flow's quasi-two-dimensionality. Reference 13 has developed such a model, hereafter SM82, by averaging the motion equations along the magnetic field lines. This results in a 2D equation where Lorentz forces appear as a linear term due to the important friction they indirectly induce by shaping the Hartmann layers (see, e.g., Ref. 26). No empirical assumptions neither empirical parameters are further required and no assumption is made on the flow quantities perpendicular to \mathbf{B} , which can be turbulent, for example. Moreover, the numerical implementation of this model only involves the addition of the linear Hartmann damping to the classical 2D Navier–Stokes equation. This model has been used in several works, some of which include turbulent flows, where it has provided results in excellent agreement with the experiments.^{1,27–29} Be-

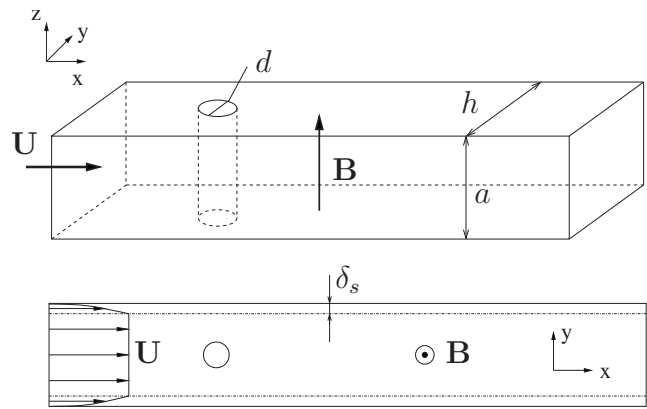


FIG. 1. (Top) Configuration of the study. (Bottom) 2D equivalent problem in the average plane to which Eqs. (1) and (2) apply.

cause it only involves 2D computations while retaining the 3D effects present in quasi-2D flows, the model from Ref. 13 can support systematic parametric investigations over a wide range of values of Re and Ha , which have not been achieved so far. Thus, the present work aims at providing a detailed description of the flow regimes with related flow visualizations and the evolutions with Re and Ha of the flow coefficients used to study the non-MHD cylinder wake. Considering the scarcity of the existing works which have dealt with the MHD cylinder wake in a strong axial external magnetic field, it constitutes a good first step that should serve as a guide for future experiments and 3D simulations.

The geometrical configuration and the flow equations are given in Sec. II. The numerical method and the validation steps are presented in Sec. III. The flow regimes and stability diagram are detailed in Sec. IV. Section V is devoted to the dynamics of the steady recirculation region and that of the unsteady vortex formation region is the subject of Sec. VI. Higher Reynolds flows are described in Sec. VII. The evolutions of the flow coefficients are given in Sec. V for the base pressure coefficient, in Sec. VI for the drag coefficient, and in Sec. VII for the Strouhal number.

II. GEOMETRY AND BASIC EQUATIONS

A. The SM82 equations

We consider a flow of the electrically conducting, incompressible eutectic alloy GaInSn (density $\rho = 6360 \text{ kg m}^{-3}$, kinematic viscosity $\nu = 3.4 \times 10^{-7} \text{ m}^2 \text{ s}^{-1}$, electrical conductivity $\sigma = 3.46 \times 10^6 \text{ } \Omega^{-1} \text{ m}^{-1}$) in a duct of square cross section past a circular cylinder. The duct walls and the cylinder are assumed to be electrically insulating. The chosen geometry (Fig. 1) is extracted from Ref. 21, the cylinder axis is at the center of the duct, and its axis is parallel to the side walls (z -axis) and orthogonal to the streamwise direction (x -axis). The duct dimensions are $a = h = 0.04 \text{ m}$. The cylinder diameter is $d = 0.01 \text{ m}$, which yields a blockage ratio $\beta = d/h = 1/4$. A steady homogeneous externally applied magnetic field \mathbf{B} with intensities between 0 and 1.35 Tesla is imposed along the cylinder axis.

In this study, the magnetic Reynolds number R_m is so

small that the induced magnetic field is negligible and the resulting magnetic field is just the imposed one $\mathbf{B} = B\mathbf{e}_z$.¹²

In such conditions, the ratios of Lorentz forces to inertia $N = \sigma a B^2 / (\rho U_0)$ (U_0 is a typical velocity that we shall define thereafter) and to viscous forces $Ha^2 = a^2 B^2 \sigma / (\rho \nu)$ are large. Thus, Lorentz forces strongly damp the velocity variations along the direction of \mathbf{B} except in the vicinity of the walls normal to \mathbf{B} . In these regions, viscous forces oppose Lorentz ones and maintain a strong velocity gradient. Thin boundary layers called *Hartmann layers* thereby develop along these walls. Their characteristic thickness is $\delta_H = a / Ha$. Thus, the flow is quasi-2D with a core region where the velocity is invariant along the direction of \mathbf{B} and thin Hartmann layers at the walls normal to \mathbf{B} . Under these assumptions, Sommeria and Moreau¹³ have derived a 2D flow model by averaging the flow equations along the direction of the magnetic field. We use the nondimensional form of this model by taking d , ρU_0^2 , and d / U_0 as respective typical length, pressure, and time,

$$\nabla_{\perp} \cdot \mathbf{u}_{\perp} = 0, \quad (1)$$

$$\frac{\partial \mathbf{u}_{\perp}}{\partial t} + (\mathbf{u}_{\perp} \cdot \nabla_{\perp}) \mathbf{u}_{\perp} + \nabla_{\perp} p = \frac{1}{\text{Re}} \nabla_{\perp}^2 \mathbf{u}_{\perp} - 2 \frac{d^2 Ha}{a^2 \text{Re}} \mathbf{u}_{\perp} + \mathbf{F}. \quad (2)$$

\mathbf{u} and p are the nondimensional averaged velocity and pressure, respectively, along the direction of the magnetic field between $z=0$ and $z=a$. $\text{Re} = U_0 d / \nu$ is the Reynolds number and $Ha = a B \sqrt{\sigma / \rho \nu}$ the Hartmann number. Quantities averaged along the magnetic field are by definition dependent only on x and y , while the subscript \perp indicates components perpendicular to the magnetic field only. The flow is put in motion by an imposed force $\mathbf{F} = F\mathbf{e}_x$. For example, this can be achieved by imposing a pressure gradient. Interestingly, the effects of the imposed magnetic field only appear in the SM82 model through a linear damping of the flow by the Hartmann layers, often called *Hartmann damping term*, with characteristic nondimensional time $t_H = a^2 \text{Re} / (d^2 Ha)$.

The boundary layers along the walls parallel to \mathbf{B} are called *Shercliff layers*. They are intrinsically 3D with a characteristic thickness $\delta_s = a / \sqrt{Ha}$. Even if the SM82 model incorrectly assimilates these particular boundary layers to 2D ones, it has been shown that the local error involved always remains below 10%.²⁷ Also, the application of the SM82 model to cases where the Shercliff layers or other parallel layers are important, has given results in excellent agreement with the experiments even when the flow is turbulent.^{1,27-29} This suggests that the three-dimensionality in the Shercliff layers is of relatively little consequence on the quasi-2D flow, so it is safe to model them using their quasi-2D counterpart for the present problem. Thus, SM82 can easily be the support of direct numerical simulations as it requires only the addition of the linear damping term to the classical 2D Navier–Stokes equation, and allows us to reduce our initially 3D problem to a 2D one.

B. Boundary conditions

We now consider the 2D problem for the quantities averaged along the z -direction sketched on the bottom of Fig. 1. The origin of the coordinate system is taken on the cylinder axis. The cylinder is impermeable and electrically insulating and so are the walls which bound the flow on the upper and lower sides. On these walls and on the cylinder circumference ∂C of equation $x^2 + y^2 = 1/4$, no-slip conditions are imposed,

$$\mathbf{u}_{\perp}(x, y = \pm h/2d) = 0, \quad (3)$$

$$\mathbf{u}_{\perp}(x, y)|_{\partial C} = 0. \quad (4)$$

The inflow boundary condition at $x = -L_u$ is derived as the exact parallel flow $\mathbf{U} = U(y)\mathbf{e}_x$ solution of Eqs. (1) and (2) for the duct flow problem without cylinder,

$$U(-L_u, y) = U_0 \frac{\cosh(yd\sqrt{2Ha/a}) - \cosh(h\sqrt{2Ha/2a})}{1 - \cosh(h\sqrt{2Ha/2a})}. \quad (5)$$

Our reference velocity U_0 is thus the maximum of the velocity profile imposed on the inflow boundary at $y=0$. The outlet boundary condition is designed so that the outflow is back to streamwise invariance. This is obtained with a Neumann condition imposed at $x = L_d$,

$$(\mathbf{n} \cdot \nabla_{\perp}) \mathbf{u}_{\perp}|_{x=L_d} = 0. \quad (6)$$

III. NUMERICAL SETUP

A. Numerical model

The flow equations (1) and (2) are solved with the finite volume code FLUENT/UNS (version 6.2) featuring a second-order upwind spatial discretization. Both steady and unsteady computations are performed. In the unsteady simulations, the time scheme is a second-order implicit pressure-velocity formulation. The equations are solved segregated and the PISO algorithm, proposed in Ref. 30 is used to solve the velocity-pressure coupling equation. A description of how the PISO algorithm is implemented in the present case is available in Ref. 28.

The additional term relating to the Hartmann damping of the flow $-(2(d/a)^2 Ha / \text{Re}) \mathbf{u}_{\perp}$ is expressed implicitly, i.e., as $-(2(d/a)^2 Ha / \text{Re}) \mathbf{u}_{\perp}^{n+1}$ at current time t^{n+1} , where \mathbf{u}_{\perp}^{n+1} is the velocity at the current time step, on which the PISO iterations are performed.²⁸ This additional term increases the flow dissipation, which results in an accelerated convergence of the numerical computations.

We use structured meshes similar to that of Ref. 4, which consists of a polar mesh embedded in a square of dimensions $3d \times 3d$ centered on the cylinder axis and a rectangular Cartesian mesh covering the resting computational domain (Fig. 2). The mesh characteristics are given in Table I and a detail of mesh M1 is shown in Fig. 2. Concerning the polar part of the mesh, the radial resolution is ruled by a geometric sequence of ratio 1.03 starting at the cylinder circumference with, typically, an initial interval for mesh M4 of about $0.008d$.

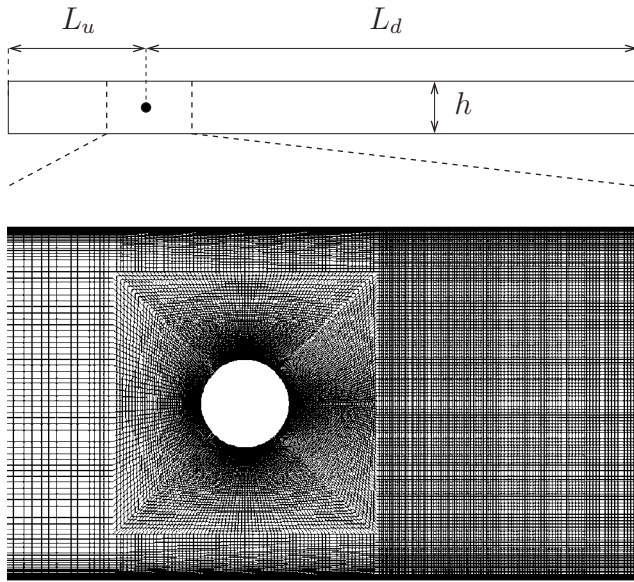


FIG. 2. (Top) Computational domain. (Bottom) Detail of the mesh around the cylinder between the dashed lines indicated on the computational domain for the M1 mesh.

Following the recommendations of Ref. 31, we take $L_u = 12$ and $L_d = 42$. The width h of the mesh is given by the blockage ratio $d/h = 1/4$. The time steps are fixed, and determined so as to satisfy the Courant–Lewy–Friedrich condition in the smallest cell of the mesh at every time step.

B. Validation of the numerical system

Few works in the literature have been dedicated to the flow past a circular cylinder in a strong axial magnetic field. Our numerical system is therefore first tested in the case of the non-MHD confined flow, for which a larger database is available. A first test is implemented to estimate the required number of mesh nodes. We perform a long-time simulation ($t = 120t_d$ with $t_d = d/U_0$) at $Re = 100$ for each mesh (Table I). We define the Strouhal number St , which is the ratio of the characteristic convection time of a vortex (d/U_0) to the period ($1/f$) of the vortex street at any given point in the wake,

and the drag coefficient C_D , which is the ratio of the drag force F_D on the cylinder acting on a unit span length to the dynamic pressure $\rho U_0^2/2$,

$$St = fd/U_0, \quad (7)$$

$$C_D = 2F_D/(\rho U_0^2 d) \quad (8)$$

and we compute the associated errors relative to M5 mesh ϵ_{st} and ϵ_{cd} (Table I). We have found that both ϵ_{st} and ϵ_{cd} decrease when the number of nodes increases, which shows good convergence. In order to save CPU time and keep a reasonable accuracy in our computations, we shall perform all our simulations with the M4 mesh.

A further test consists of finding the critical Re for the transition to the unsteady flow regime. Reference 32 has explained that a method of perturbation of the flow is required to artificially recreate the destabilizing factors always present in any experimental setup and consequently find a critical Re in agreement with experiments. Different techniques to perturb the flow can be used. In the present validation test, we perturb the flow following the same procedure as that described in Ref. 32, i.e., we let the cylinder rotate successively clockwise and counterclockwise about its own axis at the very beginning of the simulations for a short time.

The critical Re found for the transition to the unsteady regime compares well with Refs. 4 and 10 (Fig. 3), which indicates that our numerical subsystem reproduces the stability properties of the system in a very satisfactory way.

Mettu *et al.*⁸ have investigated the non-MHD confined flow past a circular cylinder using the finite volume method with FLUENT/UNS (version 6.1). The authors achieved several series of computations for $0.1 \leq \beta \leq 0.4$. In particular, they present the comparative evolutions of both St and C_D for all the implemented values of β . As can be seen in Fig. 4, our results in both St and C_D reach a very good agreement with theirs.

A final validation test was achieved for both high Re and Ha . The case from Ref. 1 with $Ha = 2400$ and $Re = 5000$ has been simulated using the present numerical model and compared with the results provided by the finite-volume based open source code OpenFOAM (version 1.4) described in Ref.

TABLE I. Main characteristics of the different meshes and errors in drag coefficient C_D and Strouhal number St relative to M5 mesh at $Re = 100$. One sees that even for the highest value of Ha , M4 insures a high enough resolution in the Shercliff layers.

Mesher	M1	M2	M3	M4	M5
Number of nodes along the cylinder circumference	120	180	260	300	360
Corresponding number of nodes in the Shercliff layers at the upper and bottom walls at $Ha = 2160$	7	10	15	16	20
Number of nodes along the radius of the embedded polar mesh	32	56	72	80	96
Total number of nodes	2×10^4	4×10^4	7×10^4	1×10^5	1.3×10^5
$\epsilon_{st} = 1 - St(Mi)/St(M5) $	3.6×10^{-2}	1.3×10^{-2}	2.6×10^{-3}	2.6×10^{-3}	/
$\epsilon_{cd} = 1 - C_D(Mi)/C_D(M5) $	5.5×10^{-3}	9.1×10^{-4}	2.8×10^{-4}	2.1×10^{-4}	/

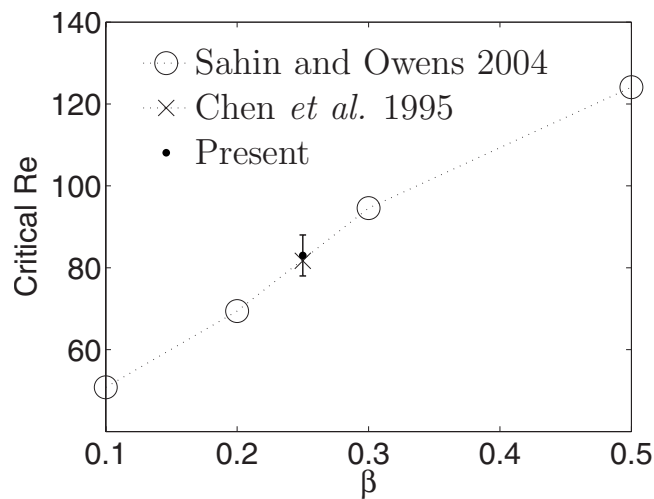


FIG. 3. Critical Re for the onset of unsteady flow regime vs the blockage ratio β . Our critical Re is located in the Re interval represented by the bar: the lower (respectively, upper) extremity is the last (respectively, first) simulation in the steady (respectively, unsteady) regime.

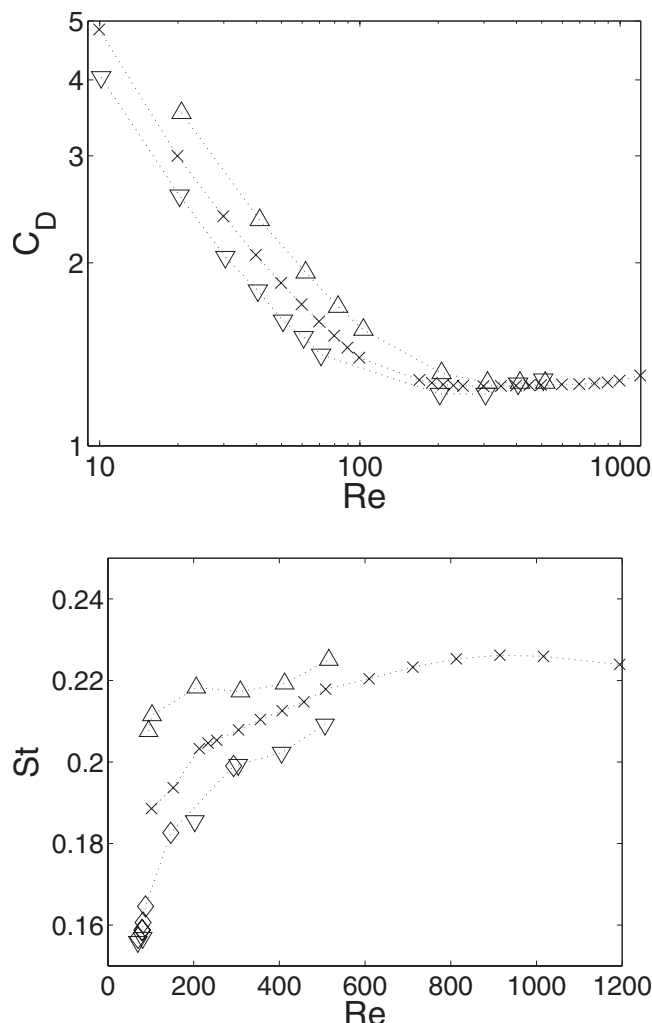


FIG. 4. [Top (respectively, bottom)] Comparative evolutions of C_D (respectively, St) vs Re . (\times) Present ($\beta=0.25$). (\diamond) Simulations from Ref. 11 ($\beta=0.2$). (∇) Simulations from Ref. 8 ($\beta=0.2$). (\triangle) Simulations from Ref. 8 ($\beta=0.3$).

33. The additional Hartmann damping term has been added in OpenFOAM in the same way as explained in the previous subsection. The same boundary and initial conditions have been implemented in both numerical packages and the computations have been achieved over the same simulation time. As a result, both codes yield flow patterns of the laminar periodic regime with the characteristic Kármán vortex street (regime III), as found in Ref. 1. The Strouhal numbers (7) given by the computations achieved with our numerical code and OpenFOAM are $St=0.2595$ and 0.2582 , respectively. From the time evolution of the vorticity at $Re=5000$ and $Ha=2400$ provided in Ref. 1 one can extract $St \approx 0.28$. Thus both codes yield very close results and the discrepancy to the experimental value must result from the numerical method itself, since the numerical and the experimental systems cannot be totally identical. Consequently, the present numerical model is able to reproduce the MHD flow past a circular cylinder even for both high Ha and Re , up to respective values of the order of 5×10^3 .

IV. STABILITY DIAGRAM

A. Flow regimes

For a given Ha , two series of numerical computations are achieved by increasing Re from 0 and decreasing Re , respectively. In the first series, once the flow reaches a fully established state, Re is slightly increased with a small step ΔRe , which is refined in the vicinity of the transition to a new flow regime. In the second series, at the transition to unsteadiness, we start with a supercritical Re and decrease it until steadiness is recovered.

Simulations have been achieved with $B=0, 0.2, 0.4, 0.7, 1.0, 1.35$ Tesla, which corresponds to $Ha=0, 320, 640, 1120, 1600, 2160$, respectively, and for Re up to about 6000. The MHD flow is fully established after a few times t_H . All our unsteady computations have been performed until this point is reached, i.e., after a total time higher than $3t_H$ and for $Ha=0$, after a total time higher than $80t_d$ ($t_d=d/U_0$). Figure 5 gives the resulting stability diagram.

It can be observed that all our MHD simulations have been performed in the area on the right-hand side of the curve corresponding to $N=10$, except for the high Re simulations in the $Ha=320$ case, where N still remains slightly lower than 10. This arbitrary value of 10 ensures that the conditions $N \gg 1$ and $Ha \gg 1$ required to have a quasi-2D flow have been effectively fulfilled and the SM82 flow model yields reliable results. For $N \sim 1$ on the left-hand side of the curve $N=10$, 3D effects are likely to appear so that the SM82 model would not be valid.

As Re is increased for a given Ha , four different flow regimes are encountered. The first three regimes are identical to the 2D non-MHD flow regimes, i.e., the creeping flow regime I, the flow of the two steady symmetric attached recirculation regions II, and the laminar periodic regime with the regular Kármán vortex street III.

We denote Re_1^c and Re_2^c the respective critical Re for the appearance of regimes II and III, respectively. For Re higher than a third critical threshold, denoted Re_3^c , the Kármán vor-

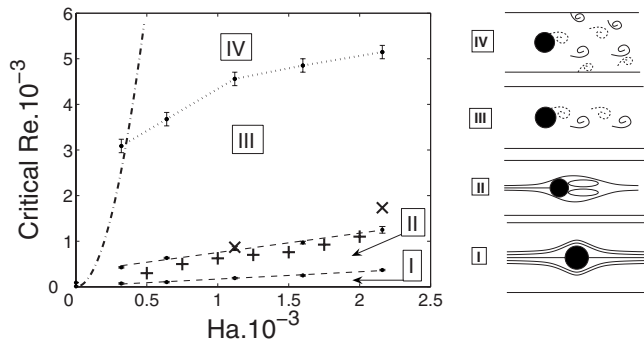


FIG. 5. Stability diagram: The sector **I** is the creeping flow regime, the sector **II** is the flow regime of the steady symmetric attached recirculation regions, the sector **III** is the laminar periodic flow regime with the regular Kármán vortex street, and the sector **IV** is the flow regime where secondary vortices are released from the side walls. $Re_1^c < Re_2^c < Re_3^c$ are the successive critical thresholds between the flow regimes. At a given Ha , each of them is located in a Re interval represented by a bar: the lower (respectively, upper) extremity is the last (respectively, first) simulation in the subcritical (respectively, supercritical) regime. The dashed lines are the respective linear regressions of Re_1^c and Re_2^c against Ha . (x) Experimental Re_2^c from Ref. 21 ($\beta=0.25$). (+) Experimental Re_2^c from Ref. 1 ($\beta=0.1$). The dashed-dotted line is the $N=10$ curve.

tex street becomes irregular. This flow regime differs from the non-MHD flow regime and we shall describe it with more details.

As seen in Fig. 6, the Kármán vortices are still generated from the rolling-up of the free shear layers as in regime **III**, but in the cylinder wake, between these vortices and the side wall layers, secondary counter-rotating vortices are generated by separation of the Shercliff layer at the side walls, shed, and eventually flow downstream. The latter vortices either cross the wake obliquely and interact strongly with the adjacent Kármán vortices or are quickly dissipated as soon as they detach from the Shercliff layer.

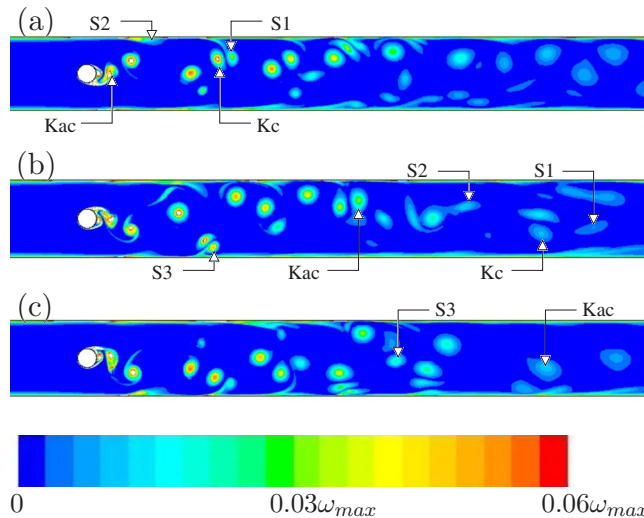


FIG. 6. (Color online) Flow regime **IV**: successive stages of the field of vorticity magnitude (s^{-1}) at $Ha=1120$ and $Re=5000$ at $t=6.44t_H$ (a), $6.67t_H$ (b), $6.90t_H$ (c). S1, S2, and S3 are secondary vortices, Kc (respectively, Kac) is a clockwise (respectively, anticlockwise) Kármán vortex. ω_{max} is the maximum vorticity magnitude.

This oblique trajectory results from the combined action of the free stream that takes them away downstream and of the Kármán vortices at the origin of their formation, that thrusts them towards the opposite side wall [see vortices S1 and Kc in Fig. 6(a)]. As a first consequence, the Kármán vortices dissipate a large amount of energy during the formation of the secondary vortices and the subsequent interaction with them. This lost energy misses downstream to further maintain the periodic vortex street. The second consequence is that the formation process of the secondary vortices disturbs the Kármán vortex street which no longer appears as a regular procession of vortices, but rather as an irregular one. Remarkably, the chaotic vortex street oscillates from one wall to the other [see Figs. 6(a) and 6(c)]. Also, since flow regime **IV** results from the presence of the side walls, the blockage ratio β is expected to play a crucial part in the transition to flow regime **IV** and for a given Ha , cases with higher β are expected to yield a lower Re_3^c .

B. Dependence on Ha

We find that the imposed magnetic field shifts the appearance of the flow instabilities to higher Re and the resulting flow regimes span over a wider interval of Re than in the non-MHD case. The reason is that the Hartmann damping shifts the exponential growth rate of the flow instabilities by Ha/Re through the linear damping action of the Hartmann layers, as seen in Eq. (2), so that a higher Re is required to effectively reach the transition to another flow regime compared to the non-MHD case as noted, for example, by Refs. 34 and 35. Thus, both transitions to flow regimes **II** and **III** are controlled by the *friction parameter* Re/Ha ,³⁶ which measures the effective ratio of inertial to Lorentz forces in quasi-2D flows. Both Re_1^c and Re_2^c obey an affine dependence with Ha for $Ha \geq 320$ with $Re_1^c \propto 0.16Ha$ and $Re_2^c \propto 0.43Ha$. In contrast, such a dependence is not so clearly observed for Re_3^c , even if an affine asymptotic one is seen for $Ha \geq 1120$ with $Re \propto 0.56Ha$. Additional computations with further values of Ha would need to be achieved to confirm this trend. Also, as in Ref. 1, no hysterical phenomenon has been found for the transition to unsteadiness.

Nevertheless, weakly supercritical simulations inside unsteady flow regime **III** present a very long transient the duration of which largely exceeds the characteristic time required by the flow to reach a fully developed state (Fig. 7).

Experimental works with configurations similar to ours^{1,21,24} have identified flow regimes **I**, **II**, and **III** and observed that the imposed magnetic field shifts the respective transitions to higher Re . We also report in Fig. 5 the experimental Re_2^c for $Ha=1120$ and 2160 provided in Ref. 21 which is in good agreement with our numerical results. On the contrary, at a given Ha , the onset of flow regime **III** occurs for a lower Re in Ref. 1 compared to ours (Fig. 5). This results from a difference in the blockage ratios, $\beta=0.1$ in Ref. 1 and $\beta=0.25$ in our simulations. Indeed, as observed in the non-MHD case, a higher blockage ratio further stabilizes the flow,^{4-6,10} which is consistent with the fact that our values for Re_2^c are higher than those of Ref. 1.

To our knowledge, only Ref. 1 has ever mentioned the

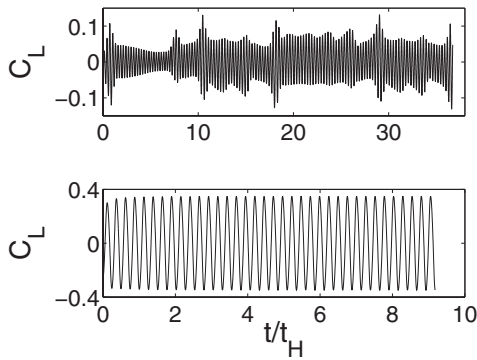


FIG. 7. (Top) Lift coefficient C_L vs t/t_H for $Ha=2160$ and $Re \approx 1.3Re_c^c$; the flow does not reach any clearly established state after almost $40t_H$. (Bottom) C_L vs t/t_H for $Ha=2160$ and $Re \approx 1.5Re_c^c$; the flow is fully established after $2t_H$. $C_L = 2F_L / \rho U_0^2 d$ with F_L lift force on the cylinder acting on a unit span length.

collapse of flow regime **III** as the Kármán vortex street becomes suddenly irregular. The authors have further explained that flow regime **IV** appears for higher Re when Ha is higher. In this flow regime, they have detected some vortices on outlying positions since they are located on positions outside of the row of the Kármán vortices with the same sense of rotation, but with different irregular streamwise velocities. Nevertheless, their observation areas only span over 1.5 diameter on either side of the wake centerline. Consequently, their recordings cannot exactly indicate the origin of the outlying vortices. Our computations show that the latter vortices actually come from the side walls [vortices S1–S3 in Figs. 6(a)–6(c)], i.e., outside of the observation areas of Ref. 1.

V. DYNAMICS OF THE RECIRCULATION REGIONS

A. Lengthening of the recirculation regions

The steady flow regime **II** is mainly characterized by the growth of two steady symmetric recirculation regions attached at the rear of the cylinder, which we shall now investigate. These regions are well characterized by their streamwise length L_b which has been shown to influence directly the base pressure coefficient C_{pb} (see, e.g., Refs. 5 and 6),

$$C_{pb} = 2(p_b - p_{0b}) / (\rho U_0^2), \quad (9)$$

p_b is the static pressure at the base point, i.e., on the wake centerline at the rear of the cylinder ($x=1/2; y=0$), and p_{0b} is the static pressure at a reference point, here on the duct axis on the inlet boundary ($x=-L_u; y=0$).

The evolutions of L_b vs Re and Ha are reported in Fig. 8 (L_b is measured on the wake centerline from the rear point of the cylinder). For each Ha , L_b is found to increase almost linearly with Re , while the slope slightly decreases with higher Ha . In addition, we have found a universal scaling law relating L_b to $Re/Ha^{4/5}$ in the limit $Ha \rightarrow \infty$ (Fig. 8). Only the curve for the case with $Ha=320$ slightly departs from this universal law, indicating a nonasymptotic regime. The critical L_b reached just before the onset of the unsteady flow regime however decreases with Ha . The MHD recirculation regions are indeed shorter than the non-MHD ones at a given

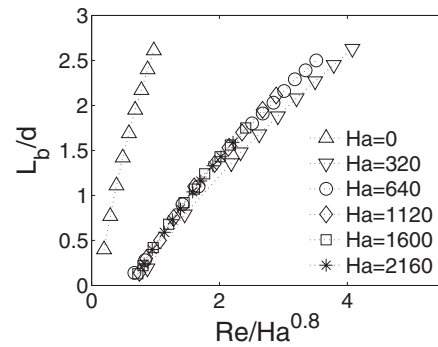


FIG. 8. Length L_b of the recirculation regions in regime **II** vs Re (non-MHD case) and universal law $L_b = f_1(Re/Ha^{4/5})$ (MHD cases). In the non-MHD case, the x -axis represents $Re \cdot 10^{-2}$.

Re and they break up at shorter lengths. So the longest recirculation regions are in fact observed in the non-MHD case.

Figure 9 shows the evolution of $-C_{pb}$ vs Re and Ha . Before the discontinuity in the slope, which corresponds to the onset of the unsteady flow regime, it can be observed that $-C_{pb}$ decreases with Re throughout the steady regimes in every tested case.

Also, $-C_{pb}$ appears to be governed by the parameter Re/Ha , and not by $Re/Ha^{4/5}$. To understand why, one can analytically compute the pressure drop induced only by the channel flow from Eq. (5), i.e., that due to Hartmann damping and viscous friction on the flow and then find the base pressure coefficient due to this pressure drop only. We shall denote it as C_{pb}^{HD} and C_{pb}^{MHD} in the non-MHD and MHD cases, respectively,

$$-C_{pb}^{HD} = 16 \frac{L_c d}{h^2} \frac{1}{Re}, \quad (10)$$

$$-C_{pb}^{MHD} = 4 \frac{L_c d Ha}{a^2 Re} \quad \text{for } Ha \gg 1 \quad (11)$$

with $L_c = (L_u + 1/2)d$.

The latter base pressure coefficients determine the evolution of $-C_{pb}$ in the creeping flow regime where the viscous and Lorentz forces dominate the flow so that the presence of the cylinder has little effect. In this regime, at a given Ha , $-C_{pb}$ decreases when Re increases as in Eqs. (10) and (11).

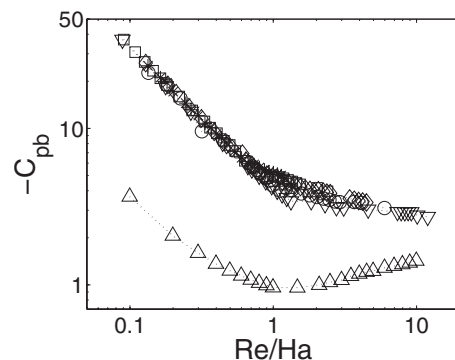


FIG. 9. Base pressure coefficient C_{pb} vs Re (non-MHD case) and universal law $-C_{pb} = f_2(Re/Ha)$ (MHD cases). In the non-MHD case, the x -axis represents $Re \cdot 10^{-2}$. Symbols have the same meaning as in Fig. 8.

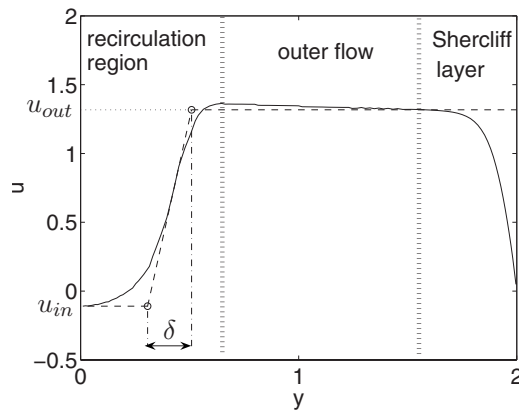


FIG. 10. Streamwise velocity profile u (solid line) vs y and derivation of δ for $Ha=1120$, $Re=588$, and $x/L_b=0.6$.

Further within the flow regime **II**, the $-C_{pb}$ curve departs little from $-C_{pb}^{MHD}$ in the MHD cases, whereas it drifts away from $-C_{pb}^{HD}$ in the non-MHD one. This shows that the pressure drop induced by the presence of the cylinder is small compared to that induced by the Hartmann damping over a length L_c of the order of magnitude of d in the MHD cases, whereas it is dominant when $Ha=0$ where no Hartmann damping is present. As a result, the MHD values of $-C_{pb}$ are all the closer to Eq. (11) as Ha is larger, which explains why Re/Ha is the governing parameter (see Fig. 9).

B. Free shear boundary layer at the outer edge of the boundary layer of the recirculation regions

In this subsection, we investigate the dynamics of the boundary layer between the recirculation regions and the main stream flow within regime **II**. The thickness δ of this boundary layer is estimated from the velocity profiles across the wake taken at regular positions inside the recirculation regions. A typical such velocity profile and the implemented procedure to derive δ are shown in Fig. 10.

The latter consists of assimilating the velocity profile to a piecewise linear profile connecting the velocity inside the recirculation regions on the wake centerline u_{in} to that of the outer flow u_{out} . The slope of this linear profile is taken at the inflection point of the real profile. δ is defined as the distance between the points where the linear profile reaches u_{in} and that where it reaches u_{out} . Moreover δ is computed along the normal to the curvature of the recirculation regions. Figure 11 shows the influence of Re over δ at $Ha=2160$, and that of Ha over δ at constant critical parameter $r=0.7$ with $r=(Re-Re_1^c)/(Re_2^c-Re_1^c)$.

Our computations show that δ is of order of the thickness of the Shercliff layer $\delta_s \sim Ha^{1/2}$, which would be equal to the absence of pressure gradients due to the streamwise variation in curvature of the boundary layer. Indeed, in the non-MHD case, the thickness of plane boundary layers parallel to the magnetic field is determined by the balance between horizontal friction and Lorentz forces. This feature of

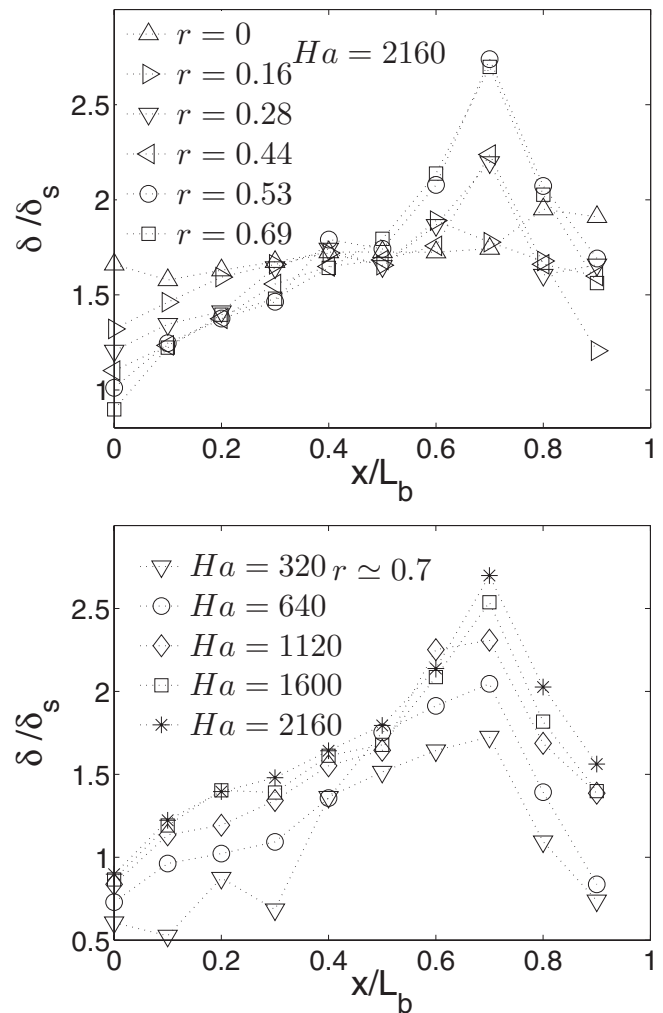


FIG. 11. (Top) Thickness of the boundary layer of the recirculation regions for increasing r at $Ha=2160$. (Bottom) Thickness of the boundary layer of the recirculation regions for increasing Ha at $r=0.7$. $r=(Re-Re_1^c)/(Re_2^c-Re_1^c)$.

the MHD flow results in a reduction of the relative importance of inertia in this region, which explains why Re_2^c strongly increases with Ha .

For a given Ha and for all values of r , δ gradually increases along the recirculation regions with a maximum thickness systematically reached at about $0.7L_b$, and eventually decreases. The maximum thickness is about $2\delta_s$ to $3\delta_s$. It can also be observed that the thickening of the boundary layer mainly takes place along the second half of the recirculation regions for $0.5 < x/L_b < 0.8$, where the curvature of the shear layer is more pronounced.

Besides, for a given r , increasing Ha roughly results in a slight shift of the curve toward higher values of δ/δ_s , while it has little influence on the general aspect of the curve. Remarkably, the position of the maximum of δ/δ_s at $x/L_b \approx 0.7$ is independent of Ha and Re over the whole range of investigated parameters. Its intensity on the other hand, increases with Re up to the point where the boundary layer breaks up and the rear of the recirculation region is released into the main stream, thus initiating the vortex street of regime **III**.

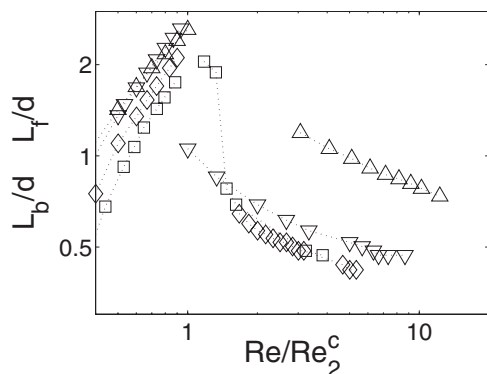


FIG. 12. Length L_b of the recirculation regions in steady flow regime **II** ($\text{Re} < \text{Re}_2^c$) and length L_f of the vortex formation region in unsteady flow regime ($\text{Re} > \text{Re}_2^c$) vs Re/Re_2^c . Symbols have the same meaning as in Fig. 8.

VI. DYNAMICS OF THE VORTEX FORMATION REGION

A. Link between the length of the vortex formation region and the pressure drop across the cylinder

As in the steady case, we shall characterize the unsteady flow regime using the recirculation length and the base pressure coefficient. In order to keep quantities consistent with the steady case, we shall only consider the time average value of C_{pb} and extend the definition of L_b . We denote the latter L_f and define it as the distance between the rear point of the cylinder on the wake centerline and that where the velocity fluctuations reach a maximum, as in Ref. 2. Figure 12 gives the evolutions of L_b and L_f for $\text{Ha} = 0, 320, 1120, 1600$ vs Re/Re_2^c .

After the almost linear increase in L_b in flow regime **II**, L_f decreases at first rather strongly and then only slightly. Moreover, at a given Re , L_f is higher when Ha is smaller and the L_f curves for $\text{Ha} = 1120$ and $\text{Ha} = 1600$ coincide very well, which indicates that a high Ha asymptotic regime is reached. Since the Kármán vortices are released at the extremity of the steady recirculation regions at the onset of the unsteady regime, the last value of L_b matches the first of L_f . As L_f suddenly drops down below $0.5d$, the vortex formation region becomes very small and the free shear layers roll up very close to the cylinder. Consequently, an oscillating boundary layer develops right at the rear of the cylinder and small vortices separate from this layer, shed and merge into the adjacent Kármán vortices or are released at the same time as the latter (Fig. 13). This formation mechanism, which is similar to that of the secondary vortices at the side walls in regime **IV**, has no significant impact on the formation mechanism of the Kármán vortices within regime **III**. In particular, none of the flow coefficients exhibit any change when these new vortices appear.

The variations of L_b and L_f can be compared to those of the base pressure coefficient C_{pb} . In Fig. 9, we present the evolutions of $-C_{pb}$ vs Re and Ha obtained from our computations. For the non-MHD case, the transition to flow regime **III** causes $-C_{pb}$ to increase again, whereas, in the MHD ones, $-C_{pb}$ still decreases after this transition even if the

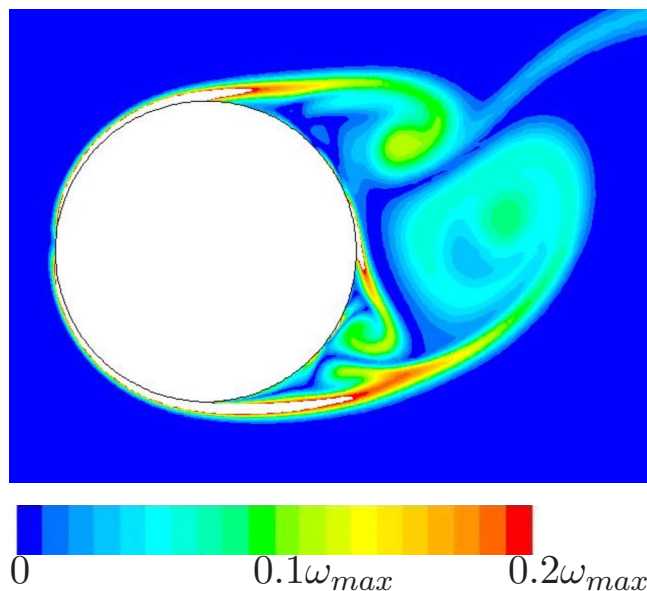


FIG. 13. (Color online) Snapshot of the field of vorticity magnitude at $\text{Ha} = 1120$, $\text{Re} \approx 2000$, and $t = 4.76t_H$. At the rear of the cylinder, a boundary layer develops and a secondary vortex grows. ω_{\max} is the maximum vorticity magnitude.

related slope still exhibits a discontinuity at the onset of flow regime **III**. It thus turns out that the decrease in L_f observed in both MHD and non-MHD unsteady regimes corresponds to an increase in $-C_{pb}$ in the non-MHD case, but to a further decrease in the MHD one. On the contrary, in the steady regime, the decrease in L_b is correlated to a decrease in $-C_{pb}$ in both cases.

To further investigate this point, let us recall that, as seen in Eqs. (10) and (11), C_{pb} strongly depends on the distance L_c between the points used to compute the pressure drop. We therefore compute another base pressure coefficient, denoted C'_{pb} , in which the point of the reference pressure is taken at the front side of the cylinder on the duct axis ($x = -1/2$; $y = 0$), which yields $L'_c = d$. Thus, C'_{pb} includes only the cylinder region and it is much less influenced by the Hartmann damping term which has been shown earlier to be the dominant part of C_{pb} . This results in C'_{pb} curves having qualitatively the same variations as those of the non-MHD curve, i.e., $-C'_{pb}$ decreases in the steady flow regime and increases in the unsteady one, as seen in Fig. 14 for $\text{Ha} = 1120$.

By comparing Figs. 12 and 14, one can observe that on the one hand, L_b increases while $-C'_{pb}$ decreases in the steady flow regime, while on the other hand, L_f decreases while $-C'_{pb}$ increases in the unsteady flow regime. In other words, $-C'_{pb}$ and L_b (respectively, L_f) have opposite relative variations in the steady (respectively, unsteady) flow regime. This link between the evolutions of the recirculation length and of the base pressure coefficient has been underlined in several works in the non-MHD case^{2,3} and is recovered in the present non-MHD computations. Thus, in both MHD and non-MHD cases, the pressure drop induced only by the presence of the cylinder starts to reduce from the onset of the unsteady regime on. While this reduction is strong enough to counteract the pressure drop imposed by the Hartmann friction over a length of the order of one cylinder diameter d , it

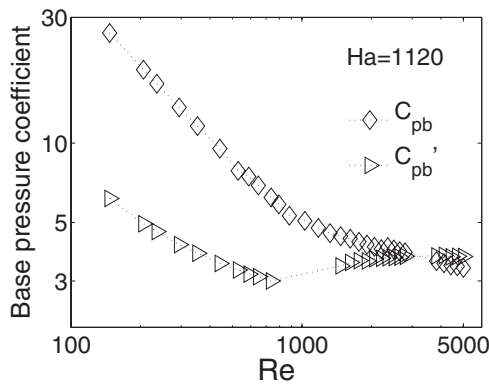


FIG. 14. Base pressure coefficient C_{pb} (respectively, C'_{pb}) vs Re at $Ha = 1120$ for a reference pressure located at the inflow boundary (respectively, at the front side of the cylinder).

is no longer the case when this length overcomes several times d . So $-C'_{pb}$ increases at the onset of the unsteady regime, while $-C_{pb}$ further decreases, even though the reduction in the slope reflects the change in pressure gradient in the close region of the cylinder at the onset of the unsteady regime.

B. Consequence on the drag coefficient

As the fluid flows over the cylinder, it exerts a force on the cylinder which results from the sum of the viscous friction and the pressure forces on the cylinder surface. By projecting this force on the streamwise direction (x -axis), one obtains the drag force. In the case of our 2D computations, the drag coefficient C_D [Eq. (8)] is thus the ratio of the drag force acting on a unit span length to the dynamic pressure. In the unsteady flow regime, we only consider the time average value of C_D . The evolutions of C_D vs Re and Ha are presented in Fig. 15.

In both non-MHD (Fig. 4) and MHD cases, we find that C_D decreases within the steady flow regimes and then increases in the unsteady ones. Nevertheless, whereas the final increase in C_D is very smooth in the non-MHD computations, a discontinuity can clearly be observed in the MHD ones before C_D starts to increase. In addition, none of the transitions to flow regimes II and IV involves any discontinuity, nor any change in the respective slopes. Finally, the

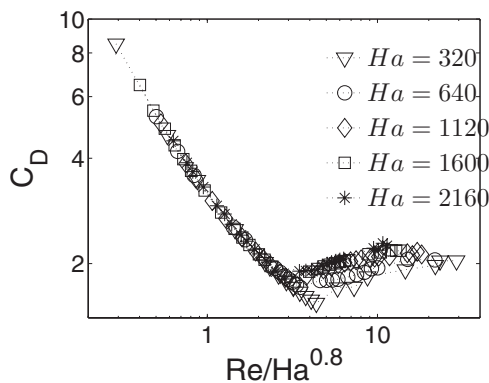


FIG. 15. Universal law $C_D = f_3(Re/Ha^{4/5})$.

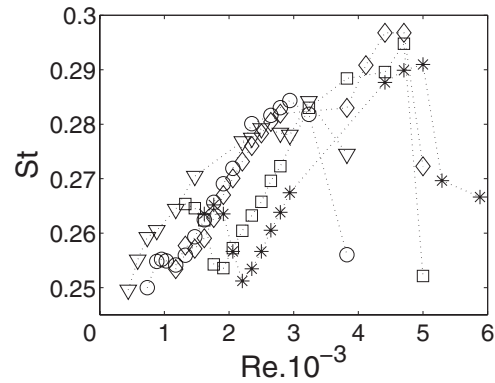


FIG. 16. Strouhal number St vs Re and Ha. Symbols have the same meaning as in Fig. 15.

MHD C_D curves tend to an asymptotic curve $C_D = f_3(Re/Ha^{4/5})$ as Ha is increased in the unsteady flow regime.

In order to understand the variations of C_D , let us now introduce the two components of the total drag coefficient $C_D = C_{D,p} + C_{D,v}$, where $C_{D,p}$ (respectively, $C_{D,v}$) is the part of C_D due to pressure (respectively, viscous) forces. In the non-MHD case with $\beta = 0$, Refs. 37 and 38 have shown that at the onset of the unsteady flow regime III, $C_{D,p}$ stops decreasing and starts to increase while $C_{D,v}$ keeps on decreasing. As a result, at the onset of the unsteady flow regime, the total drag coefficient C_D keeps on decreasing as in the steady regime, but more slowly. The increase in $C_{D,p}$ observed at the transition to unsteadiness is directly related to the base pressure coefficient. As seen in Fig. 14 with the C'_{pb} curve, the pressure drop between the rear and the front of the cylinder starts to increase after the onset of the unsteady regime and so does $C_{D,p}$, since it results from the integration of the pressure forces along the cylinder surface. Then, as the flow confinement as well as the Hartmann damping shift the transition to the unsteady flow regime to much higher Re_c^c , the effective critical threshold can be so high that $C_{D,v}$ has further vanished and can no longer counteract the increase in $C_{D,p}$. As a result, at the onset of regime III, $C_D \approx C_{D,p}$, so C_D increases in regime III, as $C_{D,p}$.

VII. HIGHER REYNOLDS FLOW

A. Drop in the Strouhal number in regime IV

The appearance of regime IV has a spectacular impact on the evolutions of the Strouhal number St [Eq. (7)] in the MHD cases.

As can be seen in Fig. 16, St increases up to a first peak value, then decreases down to a minimum value from which it increases once again up to an absolute maximum and eventually drops. The latter sudden drop in St coincides exactly with the transition to regime IV. Indeed, as a secondary vortex rises in the Shercliff layer, it sheds and begins to cross the wake during its downstream motion, and creates an obstacle that impedes the flow of the oncoming Kármán vortices [see, e.g., vortices Kc and S1 in Figs. 6(a) and 6(b)]. As a result, the vortex shedding frequency of the latter vortices decreases, leading to the observed drop in St . In contrast, as

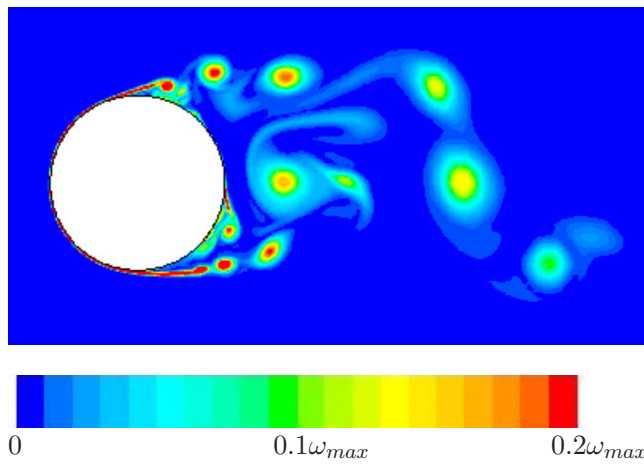


FIG. 17. (Color online) Kelvin–Helmholtz instability: snapshot of the field of vorticity magnitude at $Ha=2160$, $Re=3 \times 10^4$ and $t=9.2t_H$. ω_{max} is the maximum vorticity magnitude.

the formation of the secondary vortices occurs downstream of the cylinder, it does not affect that of the Kármán vortices. Consequently, the onset of regime **IV** has no impact on the evolutions of L_f , C_{pb} , and C_D (respectively Figs. 9, 12, and 15), since these coefficients only focus on the near wake of the cylinder. As far as we know, no work in the literature dealing with the confined flow past a circular cylinder under a strong axial magnetic field has ever provided the evolution of St with Re for a given Ha .

B. Kelvin–Helmholtz instability in the free shear layers

In this subsection, we present computations performed at $Re=3 \times 10^4$. Since no MHD experimental nor numerical data are available for comparison, these results should be regarded as qualitative only. The main purpose here is indeed to introduce a regime where instabilities take place in the free shear layers and check the validity of the 2D assumption when this happens.

We have performed computations for $Ha=2160$ at a very high Re ($Re=3 \times 10^4$) which has yielded an irregular procession of counter-rotating vortices whose formation mechanism was initiated by the Kelvin–Helmholtz (KH) instability (see Fig. 17).

Small-scale vortices are generated in the free shear layers by the KH instability and feeds a chain of KH vortices. The latter roll up at the tail of the free shear layers, merge into a large vortex which eventually breaks away and flows downstream. This mechanism is alternately generated by either free shear layer and feeds the vortex street.

$Re=3 \times 10^4$ still yields a large enough interaction parameter ($N \approx 40$) to safely assume that the large structures of the flow are quasi-2D. The vortices generated by the KH instability are however of a much smaller diameter of the order of δ_s . Reference 13 has shown that such an anisotropic structure is 2D when $N(U/U_v)(\delta_s/a)^3 \gg 1$, where U_v is the structure's velocity. When the structure is generated, it has an infinitesimal velocity, so the latter condition is fulfilled, indicating that the early growth of the structure is not affected

by 3D inertial effects, although viscous effects may give it a cigar-like shape which should not affect its 2D dynamics much. Later on, when this structure has picked up energy from the mean flow, our calculation reveals values of U_v of the order of U_0 , which for $Re=3 \times 10^4$ yields $N(U/U_v) \times (\delta_s/a)^3 \approx 4.10^{-4}$. This strongly suggests that the KH vortices may experience some disruptions because of 3D inertia, which the SM82 model is not capable of rendering. Even in the non-MHD case, where such structures are 3D, it is fairly well accepted that this vortex formation process essentially stems from a 2D mechanism.^{39,40} On this basis and taking advantage of the well defined boundary layer thickness of the MHD free shear layer, we shall now perform a simplified linear stability analysis of the latter. Since the free shear layers at the edge of the recirculation regions have been shown to be of the order of δ_s (see Sec. V), we consider the stability of two superposed fluid layers separated by a transition layer of thickness δ_s in which the velocity of streaming varies linearly from that of the upper fluid U_1 to that of the lower one U_2 .

In a first step, we do not account for the influence of the magnetic field and using Ref. 41 [p. 489 Eq. (57)], we obtain the largest growth rate σ_c related to the most unstable wavelength,

$$\sigma_c \approx 0.4 \frac{U_1 - U_2}{\delta_s}, \quad (12)$$

where $\delta_s = a/\sqrt{Ha}$ is the characteristic length of the Shercliff layers. The Hartmann damping term tends to stabilize the flow, so the laminar parallel layer is stable if t_H^{-1} is bigger than the frictionless growth rate,²⁸

$$0.4 \frac{U_1 - U_2}{\delta_s} < \frac{1}{t_H}. \quad (13)$$

We introduce $Re_{KH} = a(U_1 - U_2)/\nu$ and we obtain

$$Re_{KH} < 2.5\sqrt{Ha}. \quad (14)$$

With $Ha=1120$, for example, according to our simulations, the ratio U_2/U_1 is found to be around 5% and $U_1 \approx 1.5U_0$. This yields a critical Re_{KH} of about 58, which corresponds to Re around 15. This threshold is obviously much smaller than the observed one. This shows that additional effects such as the stabilizing influence of the curvature⁴² and the nonconstant thickness of the free shear layer play a crucial role, and ought to be incorporated in more complex analyses.

VIII. CONCLUSION

We have studied the flow of a liquid metal around a cylinder placed in a square duct under a strong homogeneous magnetic field aligned with the cylinder axis. For the high values of N and Ha we have considered, the flow can safely be assumed to be quasi-2D so we can describe it using the so-called SM82 model from Ref. 13 that reduces the problem to a 2D equation, thus opening the door to a full parametric study. At first sight, the MHD flow strongly resembles the usual 2D flow around a cylinder without magnetic field, as it exhibits the usual sequence of flow patterns when Re is increased from 0: First, a creeping flow regime, then a regime

with two steady symmetric attached recirculation regions sitting behind the cylinder and lastly the unsteady Kármán vortex street. That is about as far as the similarity goes, as in the MHD case, the transitions between these regimes are controlled by the friction parameter Re/Ha first identified by Ref. 36, leading to much higher critical Re than in the non-MHD case. Also, while those regimes are rather ideal ones without magnetic field, since the flow's two-dimensionality is difficult to reproduce experimentally, the quasi-2D MHD flow is known to be effectively achieved in our range of parameters.⁴³

Beyond the natural similarity between the MHD and the non-MHD cases, the first important differences appear in the steady regimes, where in the MHD case, the pressure drop due to the presence of the cylinder is negligible compared to that due to Hartmann friction over a duct length of the order of the cylinder diameter. Then, the free boundary layer separating the recirculation region from the outer stream is roughly that of a laminar MHD parallel layer of thickness $a/Ha^{1/2}$, whereas its non-MHD counterpart is much more dominated by inertial effects, that in both cases eventually induce the boundary layer breakup leading to the unsteady regime. Also, because all transitions occur at much higher Re in the MHD cases than in the non-MHD one, the viscous friction on the cylinder represents a much smaller part in the drag coefficient C_D , which therefore is completely controlled by its part due to the pressure forces, and increases in the unsteady MHD regime, whereas it decreases in the non-MHD case. Remarkably, both C_D and the recirculation length L_b are controlled by the parameter $Re/Ha^{4/5}$, and not by the friction parameter Re/Ha .

We have identified a new regime where vortices generated by Shercliff layer separations at the side walls interact with the Kármán vortex street to make it unstable. We have found that for high values of Ha ($Ha \geq 1120$), this regime appears for $Re \propto 0.56Ha$. To our knowledge, only the experiments of Ref. 1 reported the breakup of the Kármán vortex street at values of Re and Ha consistent with the critical values we have found in the MHD cases. We have further showed that the transition to this regime turned out to be characterized by a sudden drop in the values of the Strouhal number due to vortices separating from the wall that hamper the Kármán vortex street. Finally, we have presented one calculation at much higher Re , where the free shear layers at both upper and lower edges of the cylinder exhibited an instability of the Kelvin–Helmholtz-type, but where the local pressure gradient as well as the deformation of the layer were likely to play some key roles. Also, at such Re , N is lower, so small structures after this initial growth phase could become strongly 3D and the SM82 model can hardly provide more than some qualitative information on the 2D dynamics of the more complex 3D flow.

In summary, we have presented the first overview of the main aspects of the flow around a cylinder in a duct with an axial magnetic field and how it is altered when the two parameters Re and Ha vary. This first step in the study of this type of flow leaves many questions open, some of which will require some inevitable 3D simulations, some others can be investigated using simple but efficient 2D models. Among

those that can be answered with a 2D model is that of the influence of the walls: the transition to regime **IV** depends obviously on the blockage ratio β . Presumably, this transition will occur at lower Re for higher values of β , possibly before the transition to unsteadiness, leading to a sequence of bifurcations quite different to that presented in this study. In contrast, the effect of the weak three-dimensionality in the Shercliff and free shear layers would require a full 3D analysis for selected values of Ha and Re suggested by the 2D results of the present simulations. For the same reasons, the dynamics of the high Re Kelvin–Helmholtz vortices requires either experiments or a full 3D theory, even if a quasi-2D study of the curved free shear layer could help understand the onset conditions of this complex instability.

- ¹M. Frank, L. Barleon, and U. Müller, “Visual analysis of two-dimensional magnetohydrodynamics,” *Phys. Fluids* **13**, 2287 (2001).
- ²C. H. K. Williamson, “Vortex dynamics in the cylinder wake,” *Annu. Rev. Fluid Mech.* **28**, 477 (1996).
- ³M. M. Zdravkovich, *Flow Around Circular Cylinders* (Oxford University Press, Oxford, 1997), Vol. 1.
- ⁴J. H. Chen, W. G. Pritchard, and S. J. Tavener, “Bifurcation for flow past a cylinder between parallel planes,” *J. Fluid Mech.* **284**, 23 (1995).
- ⁵M. Coutanceau and R. Bouard, “Experimental determination of the main features of the viscous flow of the wake of a circular cylinder in uniform translation. Part 1: Steady flow,” *J. Fluid Mech.* **79**, 231 (1977).
- ⁶A. S. Grove, F. H. Shair, E. E. Petersen, and A. Acrivos, “An experimental investigation of the steady separated flow past a circular cylinder,” *J. Fluid Mech.* **19**, 60 (1964).
- ⁷W. A. Khan, J. R. Culham, and M. M. Yovanovich, “Fluid flow and heat transfer from a cylinder between parallel planes,” *J. Thermophys. Heat Transfer* **18**, 395 (2004).
- ⁸S. Mettu, N. Verma, and R. P. Chhabra, “Momentum and heat transfer from an asymmetrically confined circular cylinder in a plane channel,” *Heat Mass Transfer* **42**, 1037 (2006).
- ⁹L. Rosenhead and M. Schwabe, “An experimental investigation of the flow behind circular cylinders in channels of different breadths,” *Proc. R. Soc. London, Ser. A* **129**, 115 (1930).
- ¹⁰M. Sahin and R. G. Owens, “A numerical investigation of the wall effects up to high blockage ratios on two-dimensional flow past a confined circular cylinder,” *Phys. Fluids* **16**, 1305 (2004).
- ¹¹L. Zovatto and G. Pedrizetti, “Flow about a circular cylinder between parallel walls,” *J. Fluid Mech.* **440**, 1 (2001).
- ¹²P. H. Roberts, *Introduction to Magnetohydrodynamics* (Longmans, New York, 1967).
- ¹³J. Sommeria and R. Moreau, “Why, how, and when, MHD turbulence becomes two-dimensional,” *J. Fluid Mech.* **118**, 507 (1982).
- ¹⁴G. G. Branover, Yu. M. Gel'fgat, S. V. Turuntaev, and A. B. Tsinober, “Effect of a transverse magnetic field on velocity perturbations behind a circular cylinder swept by an electrolyte,” *Magnetohydrodynamics (N.Y.)* **5**, 41 (1969).
- ¹⁵J. Josserand, P. Marty, and A. Alemany, “Pressure and drag measurements on a cylinder in a liquid metal flow with an aligned magnetic field,” *Fluid Dyn. Res.* **11**, 107 (1993).
- ¹⁶S. J. Kim and C. M. Lee, “Investigation of the flow around a circular cylinder under the influence of an electromagnetic force,” *Exp. Fluids* **28**, 252 (2000).
- ¹⁷J. Lahjomri, P. Capéran, and A. Alemany, “The cylinder wake in a magnetic field aligned with the velocity,” *J. Fluid Mech.* **253**, 421 (1993).
- ¹⁸G. Mutschke, G. Gerbeth, V. Shatrov, and A. Tomboulides, “Two- and three-dimensional instabilities of the cylinder wake in an aligned magnetic field,” *Phys. Fluids* **9**, 3114 (1997).
- ¹⁹G. Mutschke, G. Gerbeth, V. Shatrov, and A. Tomboulides, “The scenario of three-dimensional instabilities of the cylinder wake in an external magnetic field,” *Phys. Fluids* **13**, 723 (2001).
- ²⁰H. S. Yoon, H. H. Chun, M. Y. Ha, and H. G. Lee, “A numerical study on the fluid flow and heat transfer around a circular cylinder in an aligned magnetic field,” *Int. J. Heat Mass Transfer* **47**, 4075 (2004).
- ²¹O. V. Andreev and Yu. B. Kolesnikov, “MHD instabilities at transverse flow around a circular cylinder in an axial magnetic field,” in *Third Inter-*

- national Conference on Transfer Phenomena in Magnetohydrodynamics and Electroconducting Flows, Aussois, France, 1997, pp. 205–210.
- ²²L. G. Kit, Yu. B. Kolesnikov, A. B. Tsinober, and P. G. Shtern, “Use of a conduction anemometer in investigating the MHD wake behind a body,” *Magnetohydrodynamics* (N.Y.) **5**, 46 (1969).
 - ²³L. G. Kit, S. V. Turuntaev, and A. B. Tsinober, “Investigation with a conduction anemometer of the effect of a magnetic field in the wake of a cylinder,” *Magnetohydrodynamics* (N.Y.) **6**, 331 (1970).
 - ²⁴Yu. B. Kolesnikov and A. B. Tsinober, “Two-dimensional turbulent flow behind a circular cylinder,” *Magnetohydrodynamics* (N.Y.) **8**, 23 (1972).
 - ²⁵B. Mück, C. Günther, U. Müller, and L. Bühler, “Three-dimensional MHD flows in rectangular ducts with internal obstacles,” *J. Fluid Mech.* **418**, 265 (2000).
 - ²⁶R. Moreau, *Magnetohydrodynamics* (Kluwer Academic, Dordrecht, 1990).
 - ²⁷A. Pothérat, J. Sommeria, and R. Moreau, “An effective two-dimensional model for MHD flows with transverse magnetic field,” *J. Fluid Mech.* **424**, 75 (2000).
 - ²⁸A. Pothérat, J. Sommeria, and R. Moreau, “Numerical simulations of an effective 2D model for flows with a transverse magnetic field,” *J. Fluid Mech.* **534**, 115 (2005).
 - ²⁹J. Verron and J. Sommeria, “Numerical simulation of a two-dimensional turbulence experiment in magnetohydrodynamics,” *Phys. Fluids* **30**, 732 (1987).
 - ³⁰R. Issa, “Solution of the implicitly discretized fluid flow equations by operator-splitting,” *J. Comput. Phys.* **62**, 40 (1986).
 - ³¹T. E. Tezduyar and R. Shih, “Numerical experiments on downstream boundary of flow past cylinder,” *J. Eng. Mech.* **117**, 854 (1991).
 - ³²M. Braza, P. Chassaing, and H. Ha Minh, “Numerical study and physical analysis of the pressure and velocity fields in the near wake of a circular cylinder,” *J. Fluid Mech.* **165**, 79 (1986).
 - ³³H. G. Weller, G. Tabor, H. Jasak, and C. Fureby, “A tensorial approach to computational continuum mechanics using object oriented techniques,” *Comput. Phys.* **12**, 620 (1998).
 - ³⁴A. Pothérat, “Quasi-two-dimensional perturbations in duct flows under transverse magnetic field,” *Phys. Fluids* **19**, 074104 (2007).
 - ³⁵A. Thess, “Instabilities in two-dimensional spatially periodic flows. 1. Kolmogorov flow,” *Phys. Fluids A* **4**, 1385 (1992).
 - ³⁶J. Sommeria, “Experimental study of two-dimensional inverse energy cascade in a square box,” *J. Fluid Mech.* **170**, 139 (1986).
 - ³⁷A. Thom, “The flow past circular cylinders at low speeds,” *Proc. R. Soc. London, Ser. A* **141**, 651 (1933).
 - ³⁸R. D. Henderson, “Details on the drag curve near the onset of the vortex shedding,” *Phys. Fluids* **7**, 2102 (1995).
 - ³⁹M. Braza, P. Chassaing, and H. Ha Minh, “Prediction of large-scale transition features in the wake of a circular cylinder,” *Phys. Fluids A* **2**, 1461 (1990).
 - ⁴⁰S. P. Singh and S. Mittal, “Flow past a cylinder, shear layer instability and drag crisis,” *Int. J. Numer. Methods Fluids* **47**, 75 (2005).
 - ⁴¹S. Chandrasekhar, *Hydrodynamic and Hydromagnetic Stability* (Dover, New York, 1981).
 - ⁴²W. W. Liou, “Linear instability of curved free shear layers,” *Phys. Fluids* **6**, 541 (1994).
 - ⁴³L. Bühler, “Instabilities in quasi-two-dimensional magnetohydrodynamic flows,” *J. Fluid Mech.* **326**, 125 (1996).